

Lab on a Chip

Accepted Manuscript



This is an *Accepted Manuscript*, which has been through the Royal Society of Chemistry peer review process and has been accepted for publication.

Accepted Manuscripts are published online shortly after acceptance, before technical editing, formatting and proof reading. Using this free service, authors can make their results available to the community, in citable form, before we publish the edited article. We will replace this *Accepted Manuscript* with the edited and formatted *Advance Article* as soon as it is available.

You can find more information about *Accepted Manuscripts* in the [Information for Authors](#).

Please note that technical editing may introduce minor changes to the text and/or graphics, which may alter content. The journal's standard [Terms & Conditions](#) and the [Ethical guidelines](#) still apply. In no event shall the Royal Society of Chemistry be held responsible for any errors or omissions in this *Accepted Manuscript* or any consequences arising from the use of any information it contains.



Lab on a Chip

PAPER

Microfluidic opto-caloric switch for sorting of particles with 3D-hydrodynamic focusing based on SLE fabrication capabilities

G. Meineke^a, M. Hermans^b, J. Klos^a, A. Lenenbach^a and R. Noll^a

Received 00th January 20xx,
Accepted 00th January 20xx

DOI: 10.1039/x0xx00000x

www.rsc.org/

In a miniaturised flow switch fluid flows are controlled by reducing the local viscosity via absorption of laser radiation. By this local flow rates are increased to switch the outlet port of a fluid flow carrying the analyte. The microfluidic chip is fabricated using Selective Laser-Induced Etching (SLE). SLE allows for a novel 3D-hydrodynamic focusing, realising circular shaped channel cross-sections and adapting interaction volume geometries to the profile of the laser radiation for optimised absorption. The performance of the switch is validated experimentally with dyed analyte and video image processing. The ability to sort particles like cells is demonstrated at 8 Hz with polystyrene beads having a diameter of 8 μm .

Introduction

Microfluidic switching

In the field of applications for microfluidic devices an important area is the selection and separation of single particles as e.g. drops or cells, within a mixture of other particles. Mostly known as micro total analysis systems (μTAS) or micro fluorescence-activated cell sorter (μFACS) different methods for driving the sorters have been proposed and demonstrated. The methods can be categorised in electrokinetic mechanisms, acoustophoresis, mechanical systems and optical manipulations¹. Implementing the functionality of sorting in a microfluidic chip usually increases the complexity of the set-up and the manufacturing of the chip and with it the costs. The methods in the first three categories need the most complex chips, because of integrated electrodes, mechanics, piezoelectric actuators, additional channels and ports. The fourth approach, optical manipulations, can be implemented with a simple microfluidic structure with four fluid ports, two inlets for analyte and sheath flow and two outlets for waste and collection flow. Additional ports can be limited to optical ports, for example an optical system for fluorescence excitation and detection and a second port for driving the switch. Demonstrated laser driven μFACS deployed optical scattering and gradient forces²⁻⁹, also known as optical tweezers, creation of cavitation bubbles^{10,11} or sol-gel deformation^{12,13}. The use of optical scattering and gradient forces needs complex set-ups with sophisticated optics and challenging adjustments of the laser beams because of the small foci where the forces are applied. Channel filling interference patterns⁷, moving laser foci^{4,6} or multiple laser beams² are deployed to prolong the interaction time between

laser beam and particle. In the case of sol-gel deformation and cavitation bubble generation the laser foci position is less critical, therefore the set-up can be less complex, but the chip needs to have two more ports and handling of one extra fluid is required.

Hence, for future applications a new method reducing the complexity of the system would be interesting with cheaper chips and less complex periphery.

Hydrodynamic focusing

Besides the method for driving the switch, another key functionality in μFACS is hydrodynamic focusing. By merging the analyte channel with a surrounding buffer-conducting channel the analyte flow is sheathed by buffer solution in the middle of the channel and can be narrowed down to a smaller cross section with marginal mixing with the sheath flow due to the characteristics of laminar flow. This method allows to control position and cross section of the analyte flow in a scale of a few micrometres. Moreover this reduces the risk of multiple particles passing the detection volume at the same time and makes it easier to switch the analyte flow from the waste channel to the collection channel. Analytes are confined most often in 2D, i.e. the sheath flow focuses the analyte flow in one direction, typically the horizontal one.^{11,12,14-22} This is because of the applied lithographic methods which allows fabrication of planar structures with one global depth, but gets more challenging and complex for structures with changing depths or crossing channels. Changing depths are most often generated by multi step lithography and crossing channels by building sandwich structures of several planar microfluidic layers²³. 3D-focusing in two directions, horizontally and vertically, was demonstrated using multi-layered microfluidics,^{24,25} a chimney structure,²⁶ step structures^{27,28} or chevron shaped structures²⁹ on the floor of the channel and also by use of centrifugal forces in curved channels³⁰. These methods for focusing need complex multistep manufacturing techniques and are sensitive to flow variations or focuses the analyte flow excentrically³¹ with a non-circular shape. By using

^a Fraunhofer Institute for Laser Technology ILT, Steinbachstraße 15, 52074 Aachen, Germany.

^b LightFab GmbH, Steinbachstraße 15, 52074 Aachen, Germany.

femtosecond-pulsed laser irradiation 3D-freeform microfluidic channels can be manufactured. With this approach a 3D hydrodynamic focusing was demonstrated by Paiè et al.

During the annealing step the mesoporous glass substrate shrinks ~40% in volume. With microstereolithography a liquid photoresist is polymerised level by level, building complex

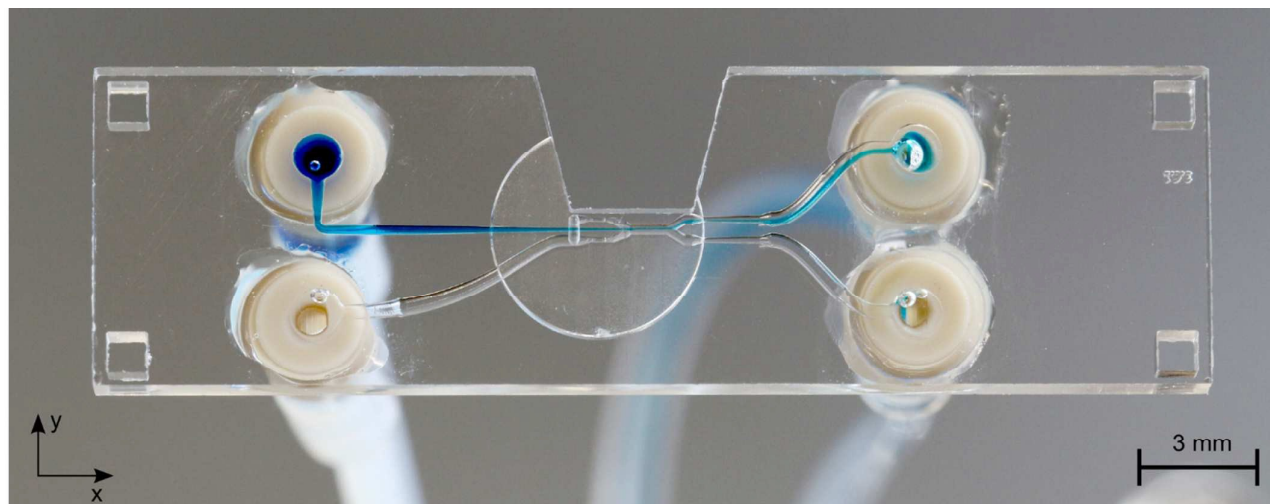


Fig. 1 Photo of the microfluidic chip with a blue dyed analyte.

enclosing the analyte flow by four surrounding sheath flows.³²

Manufacturing 3D microfluidic networks

In microfluidic networks with channels positioned at different separated layers (2.5D), the complexity of microfluidic systems can be dramatically larger than in 2D microfluidics. This is because of connections between arbitrary separated areas of the chip, without 2D routing restrictions or the need for external chip connections. 2.5D microfluidics are manufactured by stacking 2D microfluidic layers made of PDMS²⁷ (Polydimethylsiloxane, silicon based organic polymer), repetitive stacking and structuring of photosensitive SU-8 Layer³⁴ or laminating layers of polyimide and silicon³⁵. These manufacturing methods use bonding and stacking processes with high requirements regarding the positioning of each layer and the cleanliness during stacking. Consequently, assembly is often considered to be the most expensive step in microsystem processes.³⁶ A further method for manufacturing 2.5D microfluidic networks is using polymer as sacrificial layers with lithographic structuring, covering the structures with silicon or silicon nitride films, repetition of these steps for each 2D layer and finally removing the sacrificial layer by chemical dissolution or thermic decomposition³⁷. Even though 2.5D microfluidic networks are enabling more complex systems, the key elements remain in 2D like the hydrodynamic focusing section (with few exceptions²⁴⁻²⁶).

For generation of 3D microfluidic networks there were several methods demonstrated using femtosecond laser direct writing, microstereolithography and selective laser-induced etching (SLE). Femtosecond laser direct writing is a two-step process, first the fluidic network is created by femtosecond laser ablation within a mesoporous glass substrate and secondly the pores are closed by annealing. By this method the fabrication of a 3D microfluidic mixer has been demonstrated³⁸. Writing speeds of 10-100 $\mu\text{m/s}$ were achieved and after 4 repetitive exposures the 3D microchannel was machined into the glass.

objects using models set-up with computer-aided design (CAD) software. By this approach microfluidic chips³⁹ and microfluidic components like valves⁴⁰ with features as small as 50 μm have been manufactured. The polymerization process makes use of absorber and photoinitiators necessary. These substances are partially toxic and need certification for new applications in biomedical technologies.

SLE is a two-step bulk machining process at which a volume in a transparent substrate is first exposed by pulsed laser-irradiation and secondly removed by wet-chemical etching. Using this method a monolithic cell counter with 3D hydrodynamic focusing was fabricated by Paiè³. The smallest channel diameter shown from Paiè amounts to 50 μm . For the reason of chemical, thermal and mechanical resistance as well as optical transparency along with low autofluorescence, thus a high degree of biocompatibility, glass is the material chosen to be suitable for the present application. In order to machine 3D microchannel systems within glass SLE is used due to a higher productivity in comparison to fs laser direct writing within mesoporous glass. SLE is demonstrated with single exposures at writing speeds up to 200 mm/s and even several meters per second.

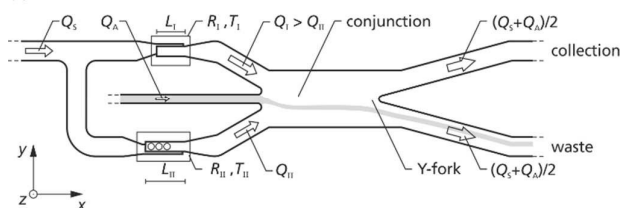
Working principle and experimental setup

Microfluidic chip design

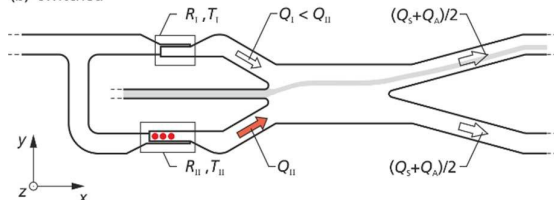
Here we present a method for microfluidic switching using a simple chip design with four ports, two inlet ports for the analyte and sheath flow and two outlet ports for the waste and the collection flow. Figure 1 shows a photo of the chip with a blue analyte flow. The chip is manufactured monolithically from fused silica by Selective Laser-Induced Etching (SLE) described below. Injecting the analyte flow in the middle of two kidney-shaped sheath flows, 3D hydrodynamic focusing is realised by vertical and horizontal confinement near the middle of the channel. The initial position of the

focused analyte flow is determined by two narrow sections I and II at an upstream position in the sheath flow channels with high hydrodynamic resistances R_I and R_{II} , see Fig. 2. The section II is designed 14 % longer than section I, such that the difference in Resistance R_I and R_{II} causes the flow rate Q_I to be larger than Q_{II} by default. Due to the larger Q_I the initial position of the analyte flow is shifted towards the negative y -direction which forms the non-switched state as depicted in Fig. 2 (a). The narrow sections are folded two times in z -direction forming a wide S-shape for optimised radiant flux absorption described below and have a cross section in the yz -plane of $30 \mu\text{m} \times 100 \mu\text{m}$, cf. Fig. 2 (c). At a subsequent Y-fork the flow is divided in approximately equal parts into the collection and the waste flow.

(a) non-switched



(b) switched



(c) cross section of region II

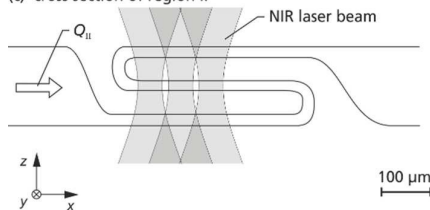


Fig. 2 Schematic design of the optocaloric switch for microfluidic sorting: two narrow sections (marked by rectangles), one in each sheath flow feed, define the ratio between the sheath flow rates Q_I and Q_{II} . The length of the narrow parts are different, with $L_I < L_{II}$ such that, due to the hydrodynamic resistances R_I and R_{II} , in the unswitched state (a) $Q_I > Q_{II}$ is sufficient to deflect the analyte flow Q_A into the waste channel. In the switched state (b) the temperature T_{II} is risen such that $Q_I < Q_{II}$ and the analyte flow is deflected into the collection channel. The narrow sections are folded two times in z -direction forming a wide S-shape (c) for optimised radiant flux absorption. The circles inside the narrow section II illustrate the positions of the laser beams irradiating this section to initiate switching.

Opto-caloric switch

Schulz et al. demonstrated in 1998 the possibility to switch an analyte flow by heating one of two sheath flow channel using electric current.¹⁹ Our new approach is to heat the sheath fluid directly by laser irradiation. In Fig. 2 the working principle is illustrated.

By direct heating of the sheath fluid in section II with laser radiation, the hydrodynamic resistance R_{II} is transiently decreased because of the lower viscosity of water at an elevated temperature. With decreasing resistance R_{II} the

hydrodynamic focusing is shifted towards the positive y -direction. If the resistance R_{II} is sufficiently decreased below R_I than the hydrodynamically focused analyte flow exits the chip completely in the collection flow. This forms the switched state as shown in Fig. 2 (b).

Due to the absorption by water, the temperature is risen directly in the channel without need for heat conduction by the surrounding chip material, allowing for a fast response of the system. Typical transition times of the sheath fluid through this narrow section are 0.2 ms to 2 ms, giving a characteristic time scale.

The opto-caloric switch shifts the whole analyte flow. Combined with an optical sensor – such as forward scattering, sideward scattering or fluorescence sensor – a sorter can be achieved, in which the shape, size and other physical properties like ductility of the particles have no significant effect on the sorting result, as long as the particles move along with the flow. This is a benefit compared to sorter concepts which utilise electrokinetic mechanisms, acoustophoresis, optical scattering or optical gradient forces for actuation.

Because of the distance between the heated narrow sections and the conjunction and because of the relatively long heating pulses, only minor pressure and temperature gradients at the particle path are exerted, compared to other, faster opto-caloric sorter concepts, for instance the one presented by Chen and Wu^{10,11}. Hence we expect that our sorter concept is less stressful for living cells. This will also cause larger switching times, which will result in lower throughput or lower downstream purity compared to faster opto-caloric sorter concepts.

Experimental setup

Figure 3 illustrates the experimental set-up. Two syringe pumps (neMESYS V2, Cetoni GmbH) drive the analyte and the

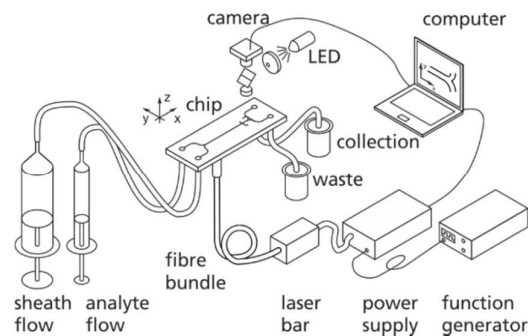


Fig. 3 Schematic layout of the experimental set-up.

sheath fluid into the chip. The chip is made of fused silica, which is transparent for the NIR-radiation used for heating. From two outlets the fluids are stored separately in a waste and collection vessel. A video camera with a microscope objective monitors the microfluidic switch.

Optical setup

For heating of the narrow section of the chip, cf. Fig. 2 (c), we use a multi-emitter laser module based on a 20 emitter AlGaIn/AsSb-laser bar (m2k-laser GmbH). Every second emitter is coupled into one multimode fibre with core diameter of $105 \mu\text{m}$ and is separately supplied by an output stage of a multi-channel power supply (Amtron GmbH).

Seven fibres are combined to a fibre bundle and the tips are glued into one ferrule. By two consecutive gradient index lenses the seven fibre tips are imaged into the chip. For heating three of the seven fibres are used, the position of the laser foci in region II are marked in Fig. 2 (a) and (b) by circles. The irradiated area of the chip is $11.780 \mu\text{m}^2$ which allows for a robust alignment.

Methods

Microfluidic channel fabrication

The 3D microfluidic chips described here are produced with Selective Laser-Induced Etching (SLE). SLE is a two-step process. In a first step ultra-short pulsed laser radiation is focused to a micrometre-sized spot and the focal spot is placed into a material which is transparent for the wavelength of the laser radiation. If the laser irradiation in the vicinity of the focal spot exceeds the threshold for non-linear ionisation effects the absorption of light generates free-carrier electrons in the conduction band of the material³³. After some picoseconds the energy is transferred from the excited electron system to the atoms and the solid is heated up to a temperature of several thousand Kelvin⁴¹. The focal spot is moved in a line-shaped way through the material and thus the material is rapidly quenched. By these processes of heating and quenching a permanent modification is being scribed into the material. This laser modification is accomplished without cracks and with a precision better than $\pm 1 \mu\text{m}$. An arbitrary volume connected in three dimensions is exposed inside the glass by 3D scanning of the laser focus. In a second step of developing only the modified material is removed by wet-chemical etching starting at a surface of the workpiece. For the precision of the SLE technique the selectivity is essential. The selectivity is the ratio of the etching rate of the modified material and the etching rate of the untreated material and is a quantity to evaluate the aspect ratio of the geometries that can be generated with SLE. Observed selectivities differ for the materials investigated so far. While for sapphire and fused silica maximum selectivities are >1000 ,⁴² newest results from LightFab show that also for soda-lime, Borofloat 33 and ULE (Ultra-Low Expansion) glass selectivities can be larger than 300. With selectivities in this range complex 3D cavities and channel systems can be produced using SLE. The basis for this is filling a volume by juxtaposing single lines, which then will be removed after etching. The SLE machining capabilities range from precision micro holes for filtering or optical applications to complex pre-mounted mechanical drives with a precision of up to $\pm 1 \mu\text{m}$ and a surface roughness of R_z down to $\sim 1 \mu\text{m}$.

For the microfluidic chip presented here the data for the line-shaped scanning of the laser focus is derived automatically from a 3D-CAD model of the chip similar to the common procedure in 3D printing. The model is sliced into layers and the generated contour lines are filled with hatch vectors to irradiate all the material which is intended to be leached out after etching. The data is transferred to the machine used for the laser inscription machine (Microscanner, LightFab with Satsuma Laser, Amplitude Systems). The lines are inscribed into a 2 mm thick fused silica wafer (SK1300, Ohara Corp.) at a wavelength of 1030 nm and an average optical power of 250 mW. After 4 days of etching in 8 mol/l KOH solution the ready-to-use chips fall out of the wafers.

Heating by laser irradiation

The radiant flux emitted by each fibre can be controlled independently and reaches in maximum more than 510 mW. The wavelength varies depending on the radiant flux used – between 1910 nm and 1940 nm – and matches an absorption band of water at 1930 nm as shown in Fig. 4. For biocompatibility we investigated the absorption of saline. Using phosphate buffered saline with Tween 20 (PBST) prepared from concentrated stock solution (Roti-Stock 10X PBST, Roth) and deionised water no significant change in absorption is found.

The heated narrow section is designed using a flat channel which is folded two times in z-direction in a way, that the laser irradiation passes the height of the channel ($30 \mu\text{m}$) three times, resulting in an absorption of about 83 % of the radiant

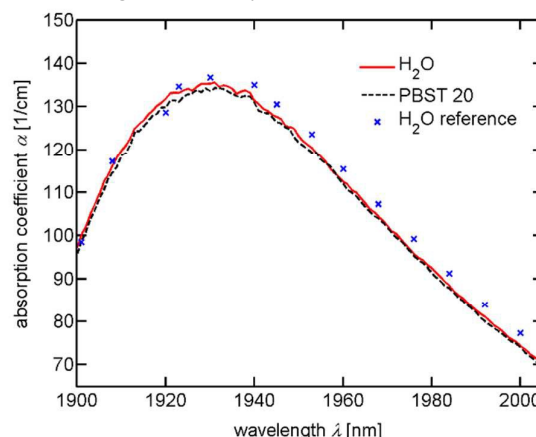


Fig. 4 Absorption of water and PBST at wavelength between 1900 nm and 2000 nm. Absorption is measured with a UV/VIS/NIR Spectrometer (Lambda 1050, PerkinElmer) using cuvettes with thicknesses of 0.01 cm and 0.02 cm and calculating the geometric mean of 4 (H_2O , solid line) respectively 3 (PBST, dashed line) measurements. For the measurements of H_2O deionised water is deployed. The reference data is taken from Kou et al.⁴³ (crosses).

flux.

Switch performance characterisation

The switch dynamic is characterised by taking images of the dyed analyte flow at the conjunction area and the Y-fork. 500 images are taken with a repetition rate ranging between 125 and 250 Hz, each image is saved with a millisecond resolved time-stamp. Laser switching is controlled by periodic TTL signals produced by a function generator (SFG-2120, GW Instek). The laser power follows a rectangular signal with frequencies from 8 Hz to 200 Hz and duty cycles from 40 % to 60 %. Improving the contrast of the analyte flow is accomplished by subtracting an image of the same section without dye. The analyte flow position is determined by fitting a Gaussian curve to the grey levels of the images along a line depicted in Fig. 5 as y-axis. Using the time stamp each image is saved with, we increase the sampling in time by sorting the images in a stroboscopic manner.

The switch response time τ is determined by fitting an exponential saturation curve $D_A(t) = D_\infty * (1 - e^{-t/\tau})$ to the rising edge of the dyed analyte flow position, with the maximum displacement D_∞ .

The maximum amount of analyte flow $Q_{A,\text{max}}$ which can be switched is estimated by determination of the maximum

displacement D_∞ of the dyed analyte flow and comparison with the total flow rate. The quantity $Q_{A,\max}$ can be estimated by integrating the cross-sectional area Ω the analyte flow could cover at the maximum displacement D_∞ without exceeding the dividing line of the Y-fork at the middle of the channel (cf. dashed vertical line in Fig. 6), weighted with the parabolic velocity field of a laminar flow, see Fig. 6 (b) :

$$Q_{A,\max} = \int_{\Omega} v_x(r) da, \quad (1)$$

$$Q_{A,\max} = (Q_S + Q_A) \left(\frac{D_\infty^2}{2B^2} - \frac{5D_\infty^4}{32B^4} \right) \quad (2)$$

with the parabolic velocity field $v_x(r)$, the sheath flow rate Q_S , the analyte flow rate Q_A , the maximum displacement D_∞ and the channel radius B and the infinitesimal area element da of the fluid cross section.

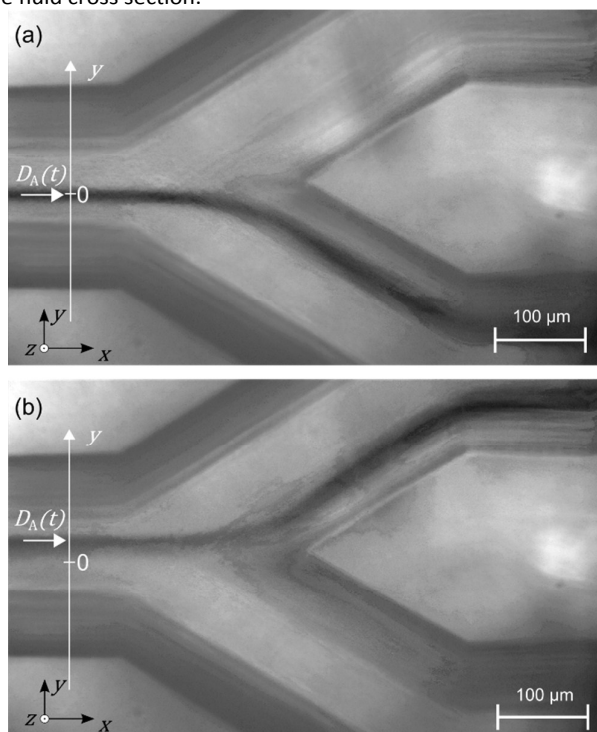


Fig. 5 Microscopic image of the (a) non-switched und (b) switched state. The analyte flow is visualised by dyeing with patent blue V. The contrast is enhanced using reference images without dyed flow. The performance of the switch is quantified by determination of the lateral y -position of the analyte flow indicated by the white arrow.

The assumption of a parabolic velocity field a simplification. In the experiment, especially at the conjunction where the flows combine, deviations of this assumption will occur. As a result of this in the experiment $Q_{A,\max}$ are observed which are higher than these estimated by up to two.

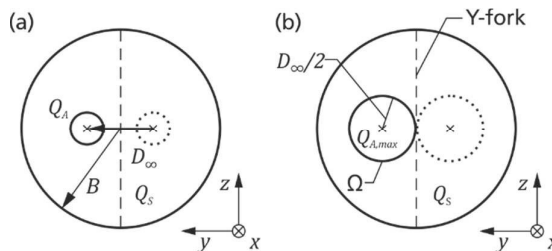


Fig. 6 Diagram to illustrate the estimation of the maximum switchable amount of analyte flow $Q_{A,\max}$. In (a) the situation of the experiment is shown to determine D_∞ and in (b) the limiting case for a maximum analyte flow $Q_{A,\max}$ is shown. The non-switched position is drawn as dashed circle, the switched state as solid circle. B radius of the channel cross section, D_∞ analyte displacement, Q_S sheath flowrate, Q_A dyed analyte flowrate, Ω cross-sectional area covered by the switchable amount of analyte flow.

Switching particles

The features of switching a flow of particles is tested with microbeads as analyte sample. The particles consist of polystyrene and have diameters of about $8 \mu\text{m}$. The images are taken with repetition rates from 55 Hz to 220 Hz and sorted using time stamps. By subtraction of a mean image, build from the preceding and the succeeding image, the particle contrast is enhanced. Using a threshold a binary image is generated and single beads are identified and their location (x_i, y_i) is determined by identifying the largest connected area big enough to be caused by a bead. The time t_c at which a bead passes the position at the left edge of the microscopic image in Fig. 5 is calculated by $t_c = t_i - x_i/v$ using the timestamp of the image t_i , the mean velocity of the flow v and the observed x -position of the particle x_i . Dependent on the y -position y_i of the identified particle, it is classified as positive (switched) or negative (non-switched). In Fig. 7 a further classification schematic is depicted. Using the time t_c of the beads and the state of the switch, the particles are classified as: I) True-positive, if they are positive and the switch is on, II) False-positive, if they are positive and the switch is off, III) False-negative, if they are negative and the switch is on and IV) True-negative, if they are negative and the switch is off. The switch is considered as being in the status on from 6 ms after the laser is switched on until the laser is switched off, cf. double arrow in Fig. 7. For each set of parameters we took three series of 500 images each. At frequencies larger than 8 Hz the time assignment of the particles is deteriorated due to increased errors caused by varying particle velocities especially after the Y-fork for particles near the inner channel wall.

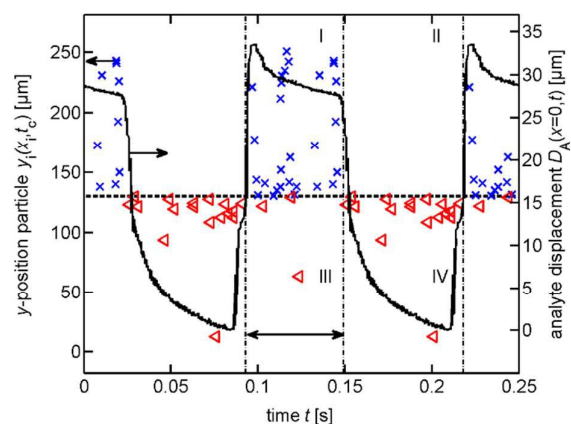


Fig. 7 Time resolved particle position and classification of particles. Depicting the y -positions of the particles at the time t_c , the ability to switch particles is estimated. Is the y -position larger than the centre of the Y-fork, plotted as dashed horizontal line, the particles are considered as switched and depicted as crosses. For y -positions smaller than the centre of the Y-fork particles are considered as non-switched and depicted as triangles. The particles are classified according to the state of the switch and the y -position. The conditions for the classification are represented as four areas: I) True-positive, II) False-positive, III) False-negative and IV) True-negative. The data shown is taken with $Q_s = 200 \mu\text{l}/\text{min}$ and $Q_a = 5 \mu\text{l}/\text{min}$ at a switching frequency of 8 Hz. For the same set of parameters the displacement D_A of the dyed analyte is plotted as solid black line, illustrating the dynamics of the switch. The data in the time interval (0,0.125s) is copied to the interval (1.25s,0.250s) to illustrate two full switching cycles.

Results and discussion

3D microfluidic features. By positioning the finest structures of the microfluidic network in the middle of the chip, the leach reaches these parts at last, which preserves the fine details. In Fig. 8 microscopic images from (b) the top (minus z -direction) and (c) from the side (minus y -direction) are seen. The 3D hydrodynamic focusing is visible as the blue analyte stream narrows down at the conjunction in the y -direction (as seen in (b)) and narrows also down in the z -direction (as seen in c). In Fig. 8 (c) also one folded narrow section with three levels is visible. The height of the middle level forms the narrowest part of the microfluidic having a channel height of $40 \mu\text{m}$. This shows the strength of SLE in manufacturing microfluidic systems with narrow parts, channels on multiple levels and combination of different channel diameters and differently shaped cross sections. The manufacturing process is still simple and does not require any assembly steps.

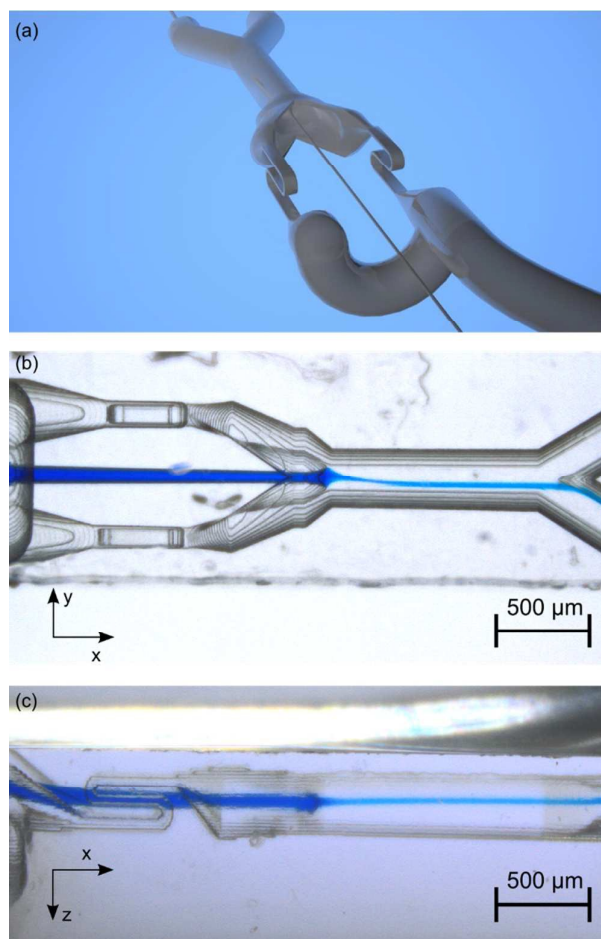


Fig. 8 Microfluidic network (a) as computer generated image and (b) top view (minus z -direction) and (c) side view (minus y -direction) of the microfluidic chip with blue analyte. The microscope images are taken at a sheath flow of $200 \mu\text{l}/\text{min}$ and an analyte flow of $5 \mu\text{l}/\text{min}$.

Switch response time. We investigated the response time for different sheath flow rates and observed a decrease with increasing flow rate, see Fig. 9. At a sheath flow rate of $50 \mu\text{l}/\text{min}$ the response time is determined to $(30.0 \pm 0.5) \text{ms}$. With increasing sheath flow rates the response time decreases to $(20 \pm 5) \text{ms}$ at $100 \mu\text{l}/\text{min}$, $(7 \pm 3) \text{ms}$ at $200 \mu\text{l}/\text{min}$ and $(5 \pm 2) \text{ms}$ at $400 \mu\text{l}/\text{min}$.

For shorter switch response times a redesign of the fluidic network is necessary. An approach is to reduce the transit time of the heated sheath flow by shortening of the narrow sections, to reduce the cross sections and to reduce the inertial mass of the sheath flow, by decreasing the length and diameter of the upstream sheath flow channels.

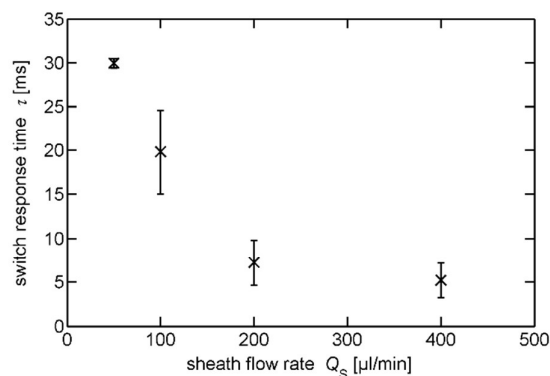


Fig. 9 Switch response times τ at different sheath flow rates Q_S . Decreasing response times at increasing sheath flow rates are observed. Error bars indicate the standard deviation of repetitive experiments.

Figure 10 (a) shows the displacement D_A at different absorbed radiant fluxes as a function of time for a sheath flow rate of 200 $\mu\text{l}/\text{min}$. At absorbed radiant fluxes above 500 mW the analyte flow displacement, determined by the Gaussian fitting routine, decreases directly after the maximum peak, which is caused by an asymmetric widening of the analyte flow starting 15 ms after onset of the heating. The widening is probably a result of the formation of vortices at the conjunction.

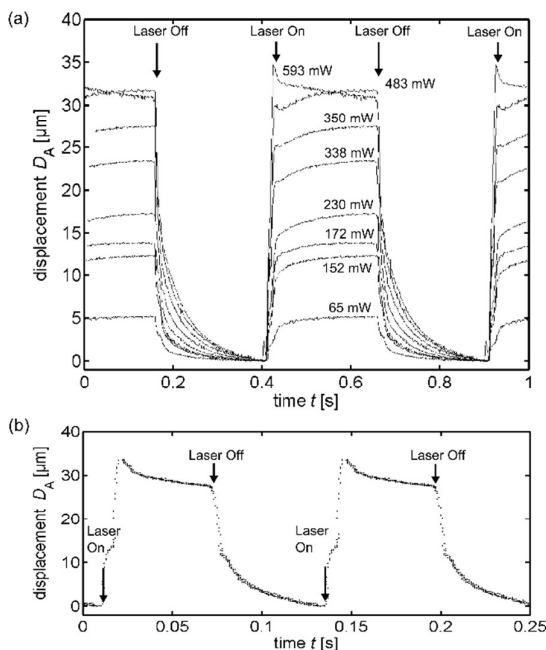


Fig 10 Displacement of the dyed analyte flow D_A as a function of time. The displacement is determined by fitting a Gaussian curve to the grey levels of images along a column, depicted in Fig. 5 as vertical y-axes. The images are captured with a timestamp and resorted to fit into one period of switching. The interval between two images is 4 to 5 ms. The data points are doubled and depicted consecutively to illustrate the periodicity. In (a) switching is executed with 2 Hz at different absorbed powers from 65 mW up to 593 mW and in (b) with 8 Hz and 736 mW. The sheath flows are (a) 200 $\mu\text{l}/\text{min}$ and (b) 400 $\mu\text{l}/\text{min}$ and the analyte flow (a) 7 $\mu\text{l}/\text{min}$ and (b) 5 $\mu\text{l}/\text{min}$.

Maximum switchable analyte flow. With increasing sheath flow rates larger flow rates of analyte can be switched and more radiant flux for heating can be used, prior formation of boiling bubbles is occurring, see Fig. 11. The maximum switchable analyte flow rates for up to 1 W absorbed radiant flux or up to the formation of boiling bubbles are 0.2 $\mu\text{l}/\text{min}$, 1.5 $\mu\text{l}/\text{min}$, 3.8 $\mu\text{l}/\text{min}$ and 6.1 $\mu\text{l}/\text{min}$ at sheath flow rates of 50 $\mu\text{l}/\text{min}$, 100 $\mu\text{l}/\text{min}$, 200 $\mu\text{l}/\text{min}$ and 400 $\mu\text{l}/\text{min}$ respectively.

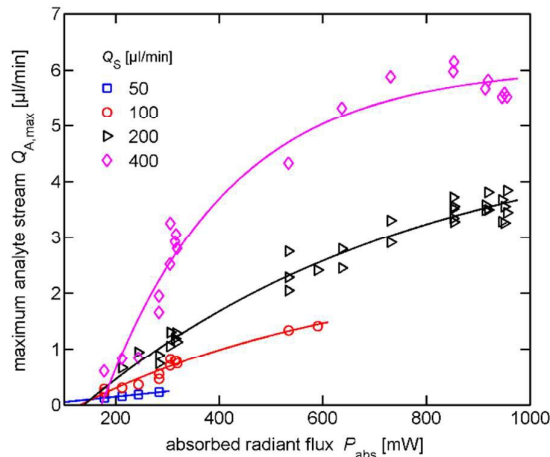


Fig. 11 The maximum analyte flow varies with the amount of absorbed radiant flux and the sheath flow rate. The data points for $Q_S = 50 \mu\text{l}/\text{min}$ and $100 \mu\text{l}/\text{min}$ are limited because of the generation of bubbles due to boiling at higher absorbed powers. The solid lines are fitted using an exponential function as guide for the eye.

Switching particles. For 200 $\mu\text{l}/\text{min}$ sheath flow, 5 $\mu\text{l}/\text{min}$ analyte flow and an absorbed optical power of ~ 740 mW we investigated switching frequencies of 4 Hz and 8 Hz. Although the theoretical value of $Q_{A,\text{max}}$ is approximately 3 $\mu\text{l}/\text{min}$, in the experiment larger values are observed. We observed (91 ± 5) % true-positive and (81 ± 9) % true-negative particles for 4 Hz. At 8 Hz switching frequency we determined (84 ± 10) % true-positive and (96 ± 8) % true-negative particles. Within the errors this values are identical. A reduction of the undesirable false-positive and false-negative is expected for larger $Q_{A,\text{max}}$. This can be done by increasing the sheath flow rate, which also increases the fluid consumption and the analyte dilution, or a redesign of the microfluidic network by increasing the hydrodynamic resistance at the narrow sections. The integration of a fluorescence sensor and triggered switching is planned for the near future, enabling shorter switching periods with higher radiant fluxes without risk of formation of boiling bubbles. Hence with triggered switching better sorting performance is expected.

Conclusions

Using the possibility to fabricate complex three-dimensional microfluidic systems by SLE, we demonstrated an optical driven switch for particle sorting. Due to the excellent optical properties of fused silica the integration of high sensitive fluorescence sensors is possible, enabling the realisation of an all-optical μFACS system with a monolithic chip. High-speed video recordings indicate the possibility to realise sorting

frequencies of up to 200 Hz at high analyte flows of 10 $\mu\text{l}/\text{min}$ †.

Acknowledgements

This work was supported by the German Federal Ministry of Education and Research (BMBF, 16SV5443K) and the Fraunhofer-Gesellschaft zur Förderung der angewandten Forschung e.V.

Notes and references

† Supporting stroboscopic video recordings at switching frequencies of 200 Hz are available online.

- 1 C. W. Shields, C. D. Reyes and G. P. López, *Lab Chip*, 2015, **15**(5), 1230.
- 2 R. Applegate, J. Squier, T. Vestad, J. Oakey and D. Marr, *Opt Express*, 2004, **12**(19), 4390.
- 3 F. Bragheri, P. Minzioni, R. Martinez Vazquez, N. Bellini, P. Paiè, C. Mondello, R. Ramponi, I. Cristiani and R. Osellame, *Lab Chip*, 2012, **12**(19), 3779.
- 4 J. Enger, M. Goksör, K. Ramser, P. Hagberg and D. Hanstorp, *Lab Chip*, 2004, **4**(3), 196.
- 5 M. M. Wang, E. Tu, D. E. Raymond, J. M. Yang, H. Zhang, N. Hagen, B. Dees, E. M. Mercer, A. H. Forster, I. Kariv, P. J. Marchand and W. F. Butler, *Nat Biotechnol*, 2004, **23**(1), 83.
- 6 X. Wang, S. Chen, M. Kong, Z. Wang, K. D. Costa, R. A. Li and D. Sun, *Lab Chip*, 2011, **11**(21), 3656.
- 7 M. P. MacDonald, G. C. Spalding and K. Dholakia, *Nature*, 2003, **426**(6965), 421.
- 8 T. D. Perroud, J. N. Kaiser, J. C. Sy, T. W. Lane, C. S. Branda, A. K. Singh and K. D. Patel, *ANAL CHEM*, 2008, **80**(16), 6365.
- 9 M. de Robert Saint Vincent, R. Wunenburger and J.-P. Delville, *Appl Phys Lett*, 2008, **92**(15), 154105.
- 10 Y. Chen, A. J. Chung, T.-H. Wu, M. A. Teitell, D. Di Carlo and P.-Y. Chiou, *Small*, 2014, **10**(9), 1746.
- 11 T.-H. Wu, Y. Chen, S.-Y. Park, J. Hong, T. Teslaa, J. F. Zhong, D. Di Carlo, M. A. Teitell and P.-Y. Chiou, *Lab Chip*, 2012, **12**(7), 1378.
- 12 K. Ozaki, H. Sugino, Y. Shirasaki, T. Aoki, T. Arakawa, T. Funatsu and S. Shoji, *Sensor Actuat B-Chem*, 2010, **150**(1), 449.
- 13 M. Haneoka, Y. Shirasaki, H. Sugino, T. Aoki, T. Arakawa, K. Ozaki, D. H. Yoon, N. Ishii, R. Iizuka, S. Shoji and T. Funatsu, *Sensor Actuat B-Chem*, 2011, **159**(1), 314.
- 14 L.-M. Fu, R.-J. Yang, C.-H. Lin, Y.-J. Pan and G.-B. Lee, *Analytica Chimica Acta*, 2004, **507**(1), 163.
- 15 H. J. Kim, H.-S. Moon, B. S. Kwak and H.-I. Jung, *Sensor Actuat B-Chem*, 2011, **160**(1), 1536.
- 16 A. J. de Mello and J. B. Edel, *J APPL PHYS*, 2007, **101**(8), 084903.
- 17 N. Pamme, R. Koyama and A. Manz, *Lab Chip*, 2003, **3**(3), 187.
- 18 T. D. Perroud, J. N. Kaiser, J. C. Sy, T. W. Lane, C. S. Branda, A. K. Singh and K. D. Patel, *ANAL CHEM*, 2008, **80**(16), 6365.
- 19 T. Schulz, S. Poser, E. M. J. Ermantraut, H. P. Mathis and J. M. Köhler, *Mesa Mg*, 1998.
- 20 Y.-C. Tung, M. Zhang, C.-T. Lin, K. Kurabayashi and S. J. Skerlos, *Sensor Actuat B-Chem*, 2004, **98**(2-3), 356.
- 21 M. M. Wang, E. Tu, D. E. Raymond, J. M. Yang, H. Zhang, N. Hagen, B. Dees, E. M. Mercer, A. H. Forster, I. Kariv, P. J. Marchand and W. F. Butler, *Nat Biotechnol*, 2004, **23**(1), 83.
- 22 B. Yao, G.-a. Luo, X. Feng, W. Wang, L.-x. Chen and Y.-m. Wang, *Lab Chip*, 2004, **4**(6), 603.
- 23 M. A. Unger, H.-P. Chou, T. Thorsen, A. Scherer and S. R. Quake, *Science*, 2000, **288**(5463), 113.
- 24 R. MIYAKE, H. OHKI, I. YAMAZAKI and T. TAKAGI, *JSME Int. J., Ser. B*, 1997, **40**(1), 106.
- 25 D. Sobek, A. M. Young, M. L. Gray and S. D. Senturia in *Proceedings An Investigation of Micro Structures, Sensors, Actuators, Machines and Systems*, ed. D. Sobek, A. M. Young, M. L. Gray and S. D. Senturia, IEEE, 1993, p 219.
- 26 A. Wolff, I. R. Perch-Nielsen, U. D. Larsen, P. Friis, G. Goranovic, C. R. Poulsen, J. P. Kutter and P. Telleman, *Lab Chip*, 2003, **3**(1), 22.
- 27 Y. Chen, A. J. Chung, T.-H. Wu, M. A. Teitell, D. Di Carlo and P.-Y. Chiou, *Small*, 2014, **10**(9), 1746.
- 28 C. Simonnet and A. Groisman, *ANAL CHEM*, 2006, **78**(16), 5653.
- 29 J. P. Golden, J. S. Kim, J. S. Erickson, L. R. Hilliard, P. B. Howell, G. P. Anderson, M. Nasir and F. S. Ligler, *Lab Chip*, 2009, **9**(13), 1942.
- 30 X. Mao, J. R. Waldeisen, and T. J. Huang, *Lab On a Chip* 7, 1260
- 31 S. Chung, S. J. Park, J. K. Kim, C. Chung, D. C. Han and J. K. Chang, *Microsyst Technol*, 2003, **9**(8), 525.
- 32 P. Paiè, F. Bragheri, R. M. Vazquez and R. Osellame, *Lab Chip*, 2014, **14**(11), 1826.
- 33 A. Vogel, J. Noack, G. Hüttman and G. Paltauf, *Appl Phys B*, 2005, **81**(8), 1015.
- 34 P. Abgrall, C. Lattes, V. Conédéra, X. Dollat, S. Colin and A. M. Gué, *J. Micromech. Microeng*, 2006, **16**(1), 113.
- 35 J. M. Yang, J. Bell, Y. Huang, M. Tirado, D. Thomas, A. H. Forster, R. W. Haigis, P. D. Swanson, R. Wallace, B. Martinsons and M. Krihak, *Biosensors and Bioelectronics*, 2002, **17**(6-7), 605.
- 36 P. Abgrall and A.-M. Gué, *J. Micromech. Microeng*, 2007, **17**(5), R15.
- 37 D. Bhusari, H. A. Reed, M. Wedlake, A. M. Padovani, S. Allen and P. A. Kohl, *J. Microelectromech. Syst.*, 2001, **10**(3), 400.
- 38 Y. Liao, J. Song, E. Li, Y. Luo, Y. Shen, D. Chen, Y. Cheng, Z. Xu, K. Sugioka and K. Midorikawa, *Lab Chip*, 2012, **12**(4), 746.
- 39 Y. Mizukami, D. Rajniak, A. Rajniak and M. Nishimura, *Sensor Actuat B-Chem*, 2002, **81**(2-3), 202.
- 40 C. I. Rogers, K. Qaderi, A. T. Woolley and G. P. Nordin, *Biomechanics*, 2015, **9**(1), 016501.
- 41 M. Hermans, J. Gottmann and A. Schiffer in *SPIE Proc Ser*, ed. F. G. Bachmann, W. Pfleging, K. Washio, J. Amako, W. Hoving and Y. Lu, SPIE, 2012, p 82440E.
- 42 M. Hermans, J. Gottmann and F. Riedel, *JLMN*, 2014, **9**(2), 126.
- 43 L. Kou, D. Labrie and P. Chylek, *Appl Optics*, 1993, **32**(19), 3531.